A Study of 28 GHz, Planar, Multi-Layered, Electrically Small, Broadside Radiating, Huygens Source Antennas

Ming-Chun Tang, *Senior Member, IEEE*, Ting Shi, *Student Member*, and Richard W. Ziolkowski, *Fellow, IEEE*

***Abstract* —Two 28 GHz, planar, electrically small Huygens source antennas are presented that are broadside radiating and are based on multi-layer PCB technology. The designs seamlessly integrate electric Egyptian axe dipole (EAD) and magnetic capacitively loaded loop (CLL) near-field resonant parasitic (NFRP) elements with a coax-fed dipole radiator. Both linearly polarized (LP) and circularly polarized (CP) systems are demonstrated. The simulations of the LP system indicate that it is electrically small: *ka* = 0.961; has peak realized gains and front-to-back ratios (FTBRs) in the range from, respectively, 3.77 to 4.54 dBi and 7.16 to 33.92 dB; and radiation efficiencies higher than 81.14% over its entire 2.14%, -10-dB fractional impedance bandwidth (FBW_{-10dB}). A prototype was fabricated and tested; the measured and simulated results are in good agreement. The CP system exhibits similar properties: *ka* = 0.942; 1.41% FBW_{-10dB} with a 0.47% 3-dB axial ratio (AR) fractional bandwidth; and peak realized gain, FTBR, and radiation efficiency values equal to 2.03 dBi, 26.72 dB, and 73.4%, respectively. To confirm their efficacy for on-body applications, the specific absorption rate (SAR) values of both the LP and CP Huygens source antennas were evaluated and found to be very low.**

***Index Terms*—Broadside radiation, directivity, electrically small antennas, Huygens source antenna, near-field resonant parasitic element, planar antennas**

Manuscript received on Sep. 26, 2016, revised on Feb. 28, 2017, and accepted on Apr. 02, 2017.

This work was supported in part by the National Natural Science Foundation of China contract number 61471072, in part by graduate scientific research and innovation foundation of Chongqing, China contract number CYS16020, in part by the Fundamental Research Funds for the Central Universities contract number 106112015CDJZR165510, in part by China Postdoctoral Science Foundation contract number 2016M590860, , in part by Funding of the Young Backbone Teachers in Colleges and Universities of Chongqing contract number 0307001104102, in part by Opening subject of State Key Laboratory of Millimeter Waves contract number K201732, and in part by the Australian Research Council grant number DP160102219.

M. -C. Tang is with the College of Communication Engineering, Chongqing University, Chongqing, 400044, China and with the State Key Laboratory of Millimeter Waves, Nanjing, 210096, China (E-mail: tangmingchun@cqu.edu.cn);

T. Shi is with the College of Communication Engineering, Chongqing University, Chongqing, 400044, China (E-mail: tingshi@cqu.edu.cn);

R. W. Ziolkowski is with the University of Technology Sydney, Global Big Data Technologies Centre, Ultimo NSW 2007, Australia, and the Department of Electrical and Computer Engineering, University of Arizona, Tucson, AZ 85721, USA (E-mail: Richard.Ziolkowski@uts. edu.au).

I. Introduction

For more than a half century, electrically small antennas (ESAs) have attracted much attention and have been extensively studied. As is well known, the overall size of an ESA, which is much smaller than its operational wavelengths, limits its directional performance. This includes characteristics such as its peak realized gain and front-to-back ratio (FTBR) [1]. Nevertheless, there have been many concerted efforts to improve an ESA's directional properties. An efficient, high directivity ESA would be valuable for many engineering applications, including, for instance, long-distance wireless energy harvesting [2], point-to-point communications [3], radio-frequency identification devices (RFIDs) [4], and on/in-body sensor systems [5]. In fact, a 28 GHz band version would meet many of the anticipated near-term goals for 5G mobile systems and IoT (internet of things) devices and their intended smart home, smart city, and cloud computing service applications [6]-[11].

Approaches to improve an ESA's directivity have included, e.g., using electromagnetic band gap (EBG) structures [12] and slot-structured conductor discs [13]; introducing two or three similar radiators to realize quasi-Yagi configurations [14, 15]; and constructing Huygens sources [16]-[25]. In particular, the Huygens source ESAs have received widespread attention due to their exceptional directional radiation performance without requiring any relatively large ground planes [12], [13] or high-profile configurations [14], [15].

According to antenna design principles, a Huygens source can be constructed with a combination of orthogonally-oriented electric and magnetic radiators that have the same excitation magnitude and phase center [16]-[19]. As a straightforward strategy, pairs of electrically small electric and magnetic dipoles with different excitation sources have been built to achieve Huygens source radiation [20]-[25]. However, as was reported in the practical designs [20], [21], the requirement of two input ports with quite different input impedances and with a certain degree of isolation between them, can inescapably lead to complicated designs and to a time consuming optimization process to align the excitation magnitudes and phase centers of the two dipoles. In contrast, there have been a variety of single-fed, planar magnetoelectric dipole antennas reported [22-24]. Unfortunately, their electrical sizes are not

small, i.e., they have $ka = 2\pi a/\lambda_0 > 1.0$, where a is the radius of the smallest sphere that completely encloses the entire antenna system at its operational wavelength λ_0. As an alternative, we have recently achieved several single-feed, electrically small, near-field resonant parasitic (NFRP) [26] Huygens source antennas, e.g., coplanar stripline (CPS)-fed, end-fire radiating [20]; low profile, broadside radiating [19], [25]; and broader bandwidth non-Foster [27] versions. While these UHF-band, single-feed Huygens source ESAs are simple in design, nearly completely impedance matched to their source generators, exhibit high directivity and FTBR values, and have high radiation efficiencies, their configurations were not tailored to high frequency fabrication approaches and design methodologies.

Because high directivity is a known desirable attribute for upcoming 5G mmWave systems, easily fabricated, low-cost, planar, single-feed, Huygens source ESAs would be very appealing for many conjectured 5G applications. Arrays generating higher gain steerable beams are desired. In the selection of the unit element to achieve a compact array for integration with a 5G mobile platform, an ESA with high directivity and high FTBR values would be an attractive candidate [28]. Moreover, in a variety of IoT application scenarios, such as 5G on-body sensors, there exists unavoidable close contact between the human body and the antenna. Consequently, an ESA with high broadside radiation performance, high FTBR values, *and* low SAR (specific absorption rate) values is very highly desired [29]. Finally, with the development of integrated packaging technologies, planar antennas, which could be easily fabricated using multi-layer PCB, LTCC, and MMIC technologies, have become increasingly indispensable for future 5G systems.

For the higher frequency initial 5G roll-out, the nascent 28 GHz band has attracted substantial interest. In this paper, linearly polarized (LP) and circular polarized (CP), 28 GHz band, single-feed, planar, Huygens source NFRP ESAs are reported. In Section II, a coaxially-fed, linearly polarized (LP), Huygens source NFRP ESA is introduced that was designed for fabrication with microwave multi-layer PCB manufacturing technologies. This LP Huygens source NFRP antenna was fabricated and tested. The measured results are in good agreement with their simulated values. They demonstrate that it is electrically small ($ka = 0.966$) and provides a 3.96 dBi peak realized gain and a 33.92 dB peak FTBR in the 28 GHz band with more than 81% radiation efficiency. Moreover, the SAR values of this antenna are studied numerically at different positions on the human body, demonstrating its very low SAR properties. Next in Section III, the LP design principles guide the modification of the NFRP elements to accomplish a coaxially-fed, CP Huygens source NFRP ESA. Its performance characteristics and SAR properties are also evaluated numerically. Both exceptional radiation performance characteristics and low SAR properties are demonstrated. Finally, some conclusions are drawn in Section IV.

All of the electromagnetic simulations were performed with the frequency domain ANSYS/ANSOFT High Frequency Structure Simulator (HFSS) [30] and were then confirmed with the time domain CST Microwave Simulator (MWS) tool set [31].

II. LP Huygens Source ESA

The geometry and the design parameters of the proposed LP Huygens source ESA are illustrated in Fig. 1. The multi-layered nature of the design is highlighted. The corresponding optimized design parameters are given in Table I.

A. LP Design

As shown in Fig. 1, the LP Huygens source ESA is a four-layer PCB design. It is constructed step-by-step in a manner analogous to those realized in the UHF band [25]. The pieces of the magnetic and electric NFRP elements and the driven element were all printed on Rogers Duroid™ 5880 substrates that had a 0.5 oz (0.017mm) copper cladding and whose relative dielectric constant $\varepsilon_r = 2.2$, relative permeability $\mu_r = 1.0$, and loss tangent $\tan \delta = 0.0009$. These material properties are valid in the frequency range 8-40 GHz [32].

The transverse physical sizes of the substrate slabs are the same and quite small: L×W= 2.0 mm × 2.4 mm. A rectangular copper patch with the size L1×W1 lies on the upper side of substrate Layer_1. Two same-sized smaller rectangular copper patches (the total transverse size of these two patches and the gap, g1, between them is the same as the upper copper patch) are located on the lower side of Layer_2. With these small sizes, the antenna fabrication, assembly, and soldering processes are difficult. As a consequence, certain design strategies were taken into consideration. First, two pairs of copper pads were etched on the lower side of Layer_1 and two more were etched on the upper side of the Layer_2. This approach guaranteed alignment of the four vertical via holes through Layer_1 and Layer_2. The patches and these pads were attached using R1 = 0.15 mm radius vias. Consequently, the pads maintained the desired electrical connectivity of the vias at the interface between the Layer_1 and Layer_2, even if these slabs incurred a small displacement during their assembly. Furthermore, the via-pad assembly provided additional mechanical support for Layer_1 and Layer_2.

The resulting patch-via structure acts as a magnetic NFRP element. It can be regarded as an extruded CLL structure analogous to the one used in the 3D magnetic EZ antennas [26] and the ones used in previous Huygens source ESAs [19], [25], [27]. The currents on this CLL element are resonantly driven into a loop mode by the x-directed currents on the dipole element. Thus, it produces a magnetic dipole oriented along the y-axis. The simulated 3D directivity pattern produced by this combination is shown in the subplot in Fig. 1(a).

The straight-segment "I" version of the curved EAD NFPR element used previously [18], [19], [25], [27], is placed between the patches on the top of Layer_2. The dipole element drives x-directed currents on it; and, hence, it produces an electric dipole oriented along the x-axis. The simulated 3D directivity pattern produced by this combination is shown in the subplot in Fig. 1(a). The vertical position of this electric NFRP

element is important; its placement allows the alignment of its phase center with that of the magnetic NFRP element [19]. Therefore, the thicknesses of Layer_1 (h1) and Layer_2 (h2) are not the same. They are adjusted to achieve this alignment.

Layer_3 is bare and acts as a spacer slab between the two NFRP elements and the driven element. Its thickness is adjusted to achieve the requisite level of coupling between the driven and NFRP elements. To ease the manual assembly, all of the substrates were adhered together using a silicone rubber adhesive. Clearly, the latter would not be present in a commercial PCB fabrication process.

In contrast to the single-layer driven dipole element used previously [18], [19], [25], [27], the coax-fed dipole is designed, as shown in Fig. 1(d), to lie on both interfaces of Layer_4. Two metallic strips and an annular pad are placed on the upper and lower sides of Layer_4, respectively. Two metallic via holes with radius R3 = 0.145 mm were drilled through the substrate. The longer strip (with the length W5) is connected to the annular pad through one via, and the shorter strip (with the length W6) is directly connected to the inner conductor of the 50 ohm coaxial feed-line by a via through a same-sized hole in the substrate. Concomitantly, the annular copper pad is designed larger than the outer conductor size of the coaxial feed-line and is directly soldered to its outer conductor. It was found that this specially engineered annular pad provided superior connection/soldering room for the outer conductor of the feed-line than the noted one-layer printed dipole used in the previous UHF designs.

In order to accommodate the antenna's physically small size, a KTG 047-50 type, semi-rigid, 50Ω coaxial cable, having a 109 GHz cut-off frequency, from Shenzhen Kansai Industrial LTD, was selected to feed it. Its inner conductor diameter was only 0.29 mm. Thus, the final manual assembly required great care with all of these small dimensions.

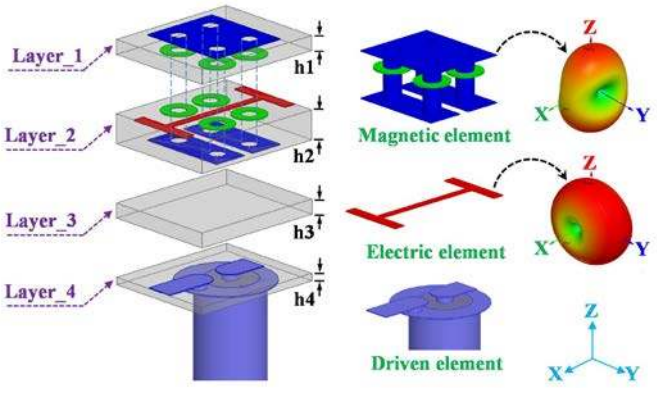

(a)

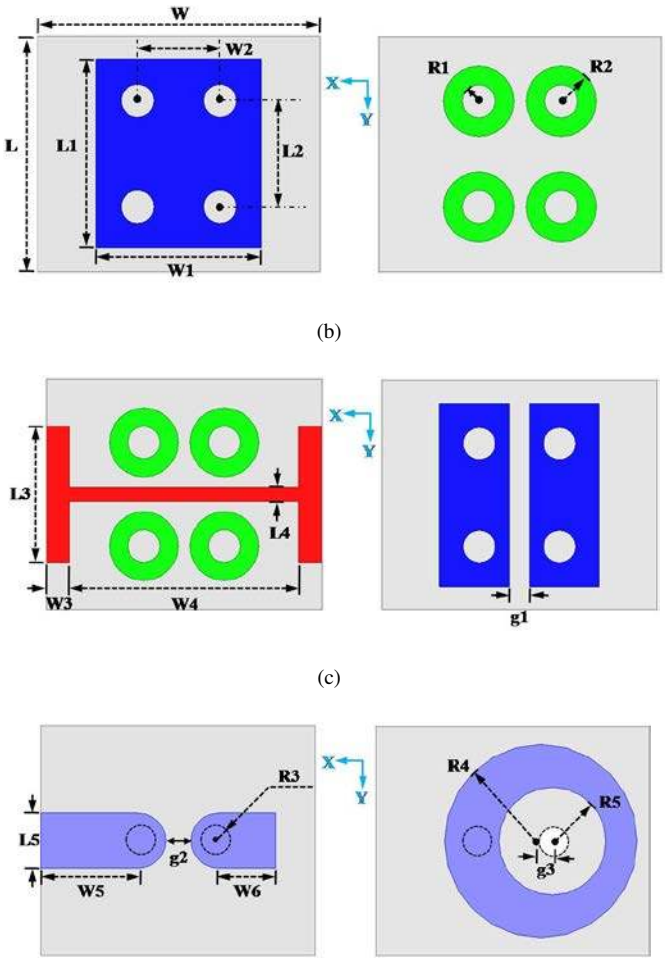

(b)

(c)

(d)

Fig. 1 Geometry of the LP Huygens source ESA. (a) 3-D isometric view, (b) upper and lower surfaces of Layer_1, (c) upper and lower surfaces of Layer_2, and (d) upper and lower surfaces of Layer_4.

TABLE I. OPTIMIZED LP HUYGENS SOURCE ESA PARAMETERS (IN MM)

h1=0.254	*h2=0.508*	*h3=0.254*	*h4=0.127*
L=2	*L1=1.6*	*L2=0.9*	*L3=1.18*
L4=0.127	*L5=0.48*	*W=2.4*	*W1=1.4*
W2=0.7	*W3=0.20*	*W4=2*	*W5=0.85*
W6=0.5	*g1=0.18*	*g2=0.22*	*g3=0.1*
R1=0.15	*R2=0.3*	*R3=0.145*	*R4=0.845*
R5=0.47	*NULL*		

B. Simulated and Measured LP Results

The components of the LP antenna in Fig. 1 were fabricated and assembled. Three prototypes were tested: each had the same antenna, but different coax-cable lengths to compensate for any source current leakage during the measurements. Photos of these fabricated prototypes are given in Figs. 2(a); a top zoom-in on the radiating element is given in Fig. 2(b). The antenna performance characteristics were simulated and obtained experimentally. The reflection coefficient was measured using an Agilent E8361A PNA vector network

analyzer (VNA) having a potential measurement scale 0.01–67.0 GHz.

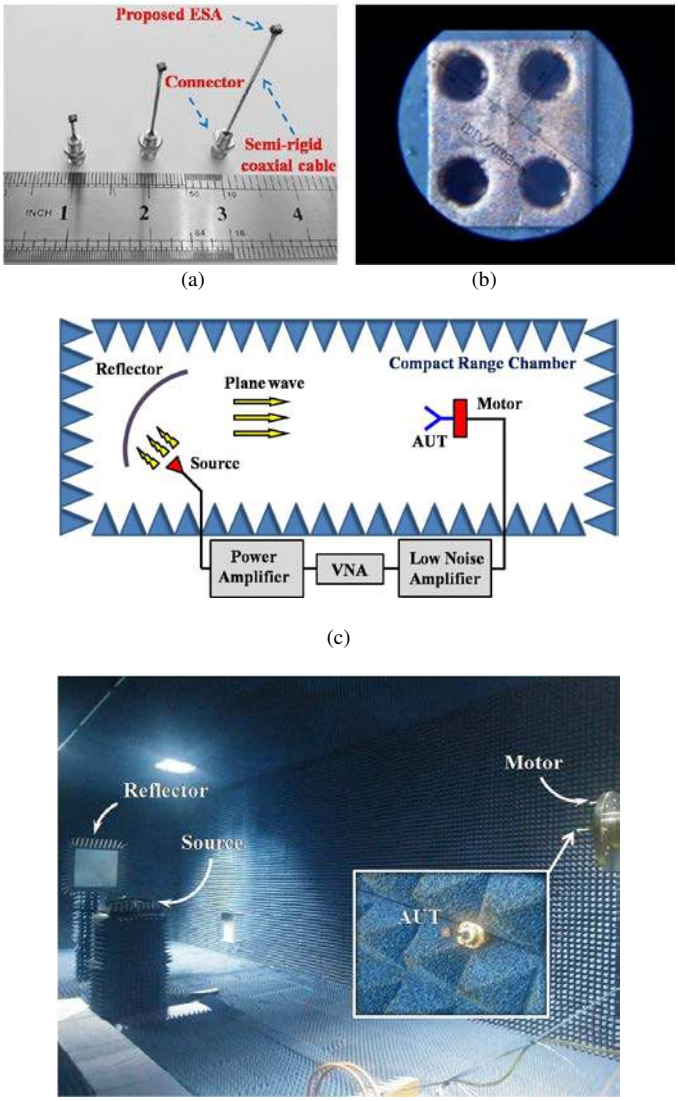

Fig. 2 Fabricated LP Huygens source ESA. (a) 3-D isometric view of the three prototypes attached to different lengths of the semi-rigid coaxial cable, (b) top zoom-in view of one prototype under a MG10085-1A 100X reading microscope, and (c) antenna under test (AUT) measurement setup diagram, and (d) AUT radiation pattern measurement setup.

The measured $|S_{11}|$ values together with the corresponding HFSS and CST simulated values are plotted in Fig. 3 (a). The CST and HFSS simulated $|S_{11}|$ values agree very well. The measured (simulated) -10dB impedance bandwidth is 350 MHz, from 27.74 to 28.09 GHz (600 MHz, from 27.66 to 28.26 GHz). Some minor, but distinct differences between the simulated and measured results were observed. Simulations have shown that the magnetic NFRP element makes stronger contributions at lower frequency points while the electric NFRP element makes stronger contributions at higher frequency points relative to the HFSS predicted system resonance frequency point, 27.835 GHz, at which $|S_{11}|_{min}$ ~ -20 dB. Moreover, the simulations clearly demonstrate a very good overlap of these resonance effects at that point. This contributes to the large simulated (measured) total -10-dB impedance bandwidth, 600 MHz (350 MHz), corresponding to a -10-dB fractional impedance bandwidth: FBW_{-10dB} = 2.2% (FBW_{-10dB} = 1.3%).

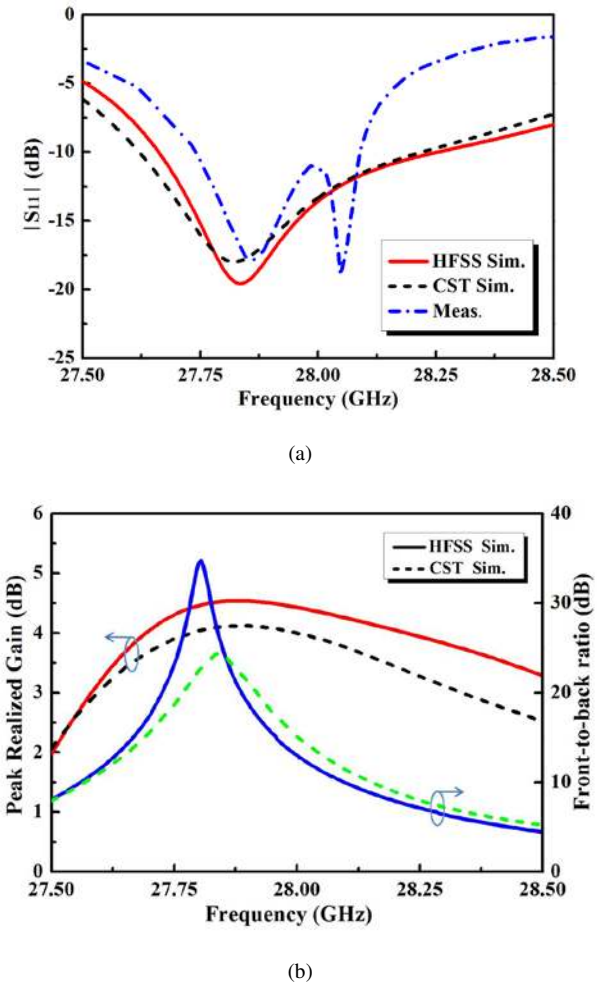

Fig. 3 The HFSS (solid line) and CST (dash line) simulated, and the measured (dash dot line) performance characteristics of the LP Huygens source ESA. (a) $|S_{11}|$ values versus frequency, and (b) peak realized gain and and FTBR values versus frequency.

On the other hand, the measured prototype antenna results show that the overlap did not completely occur as predicted. They indicate that the magnetic and electric NFRP elements have distinct resonance frequency centers, respectively, at 27.86 and 28.05 GHz. Because these centers had more separation than expected, the overall system had a narrower impedance bandwidth ~ 350 MHz. These differences between the simulated antenna models and the measured prototype are mainly a consequence of the tolerances associated with the fabrication of its components and assembly processes. While some are a result of inevitable minor errors associated with the latter and the measurement process itself, one major factor was the fact that the prototype ESA was assembled by adhering together the four substrates with the silicone rubber adhesive. While the rubber layers were expected to be quite thin, they

caused a 0.09 mm increase in the height of the system, which was not considered in the original simulations. Subsequent studies have confirmed that the height increase caused by the adhesive did negatively impact the outcomes as noted.

Because this adhesive issue was itself uncertain at the time of assembly, it was not possible to anticipate the final height in the design simulations and compensate for the presence of the adhesive. Despite the resulting decrease in the predicted bandwidth, the measured operational frequency range still covers a good portion of the local multipoint distribution system (LMDS) band [33] and overlaps nicely with the bandwidth defined for the Samsung 5G prototype mmWave antennas (520 MHz signal bandwidth centered on the 27.925 GHz carrier frequency) [34]. Furthermore, these results confirm that the Huygens source antenna is electrically small. Its measured (simulated) overall electrical size at the lowest frequency in its operational band gives ka = 0.966 (0.961).

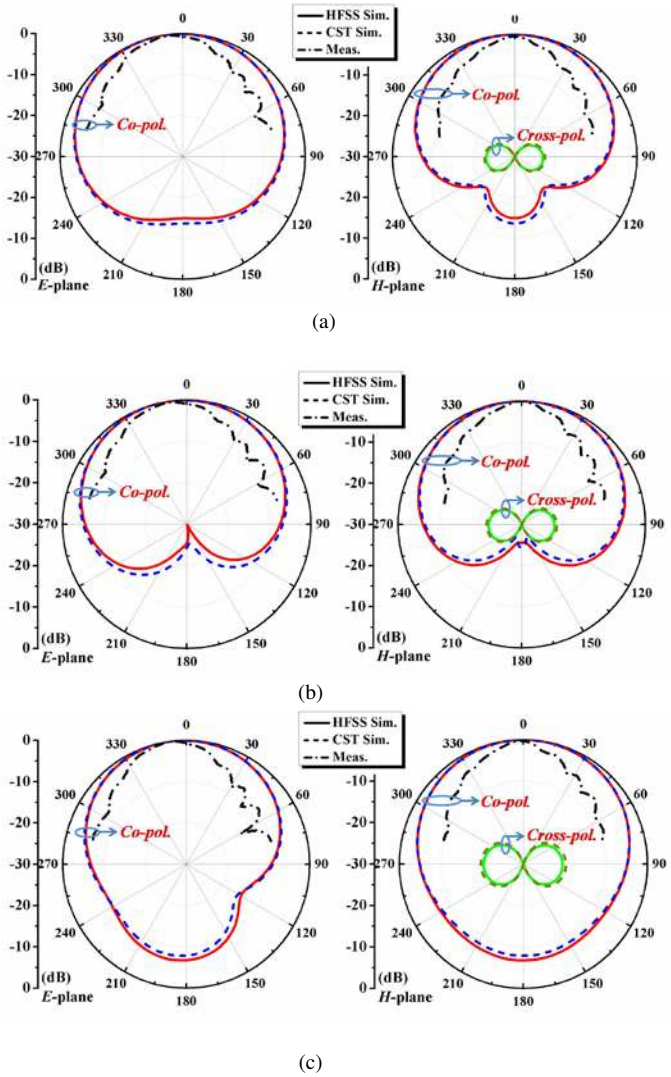

Fig. 4 The HFSS (solid line) and CST (dash line) simulated, and the measured (dash dot line) 2-D realized gain patterns of the LP Huygens source ESA. (a) At the lower operational frequency bound (27.66 GHz in simulation and 27.74 GHz in measurement, (b) at the center frequency (27.835 GHz in simulation and 27.9 GHz in measurement), and (c) at the higher operational frequency bound (28.26 GHz in simulation and 28.1 GHz in measurement).

The far-field radiation patterns were measured in a compact range chamber measurement system. The measurement setup diagram and the corresponding measurement environment are shown in Figs. 2(c) and 2(d). When arriving at the reflector, the linearly polarized expanding wave from the source (a calibrated horn antenna) is transformed into a plane wave and delivered to the antenna under test (AUT). Thus the AUT is measured as a receiving antenna. Due to limitations of the measurement system, only the angular range within ± 75° of the co-polarized radiation patterns was measured.

The HFSS (CST) predicted peak realized gain and FTBR results are shown in Fig. 3(b) for three frequencies within the -10-dB impedance bandwidth. The peak realized gain is in the range from 3.77 to 4.54dBi (3.24 to 4.12 dBi). The maximum value is located at 27.88 GHz (27.9 GHz). The FTBR and radiation efficiency (RE) values are in the range from 7.16 to 33.92 dB (from7.83 to 27.7 dB) and from 81.14 to 89.76% (from 81.41 to 89.69 %), respectively. The measured peak realized gain is 3.96 dBi at 28 GHz. In general, the difference in the simulated and measured peak realized gain values are deemed small and acceptable, e.g., during the entire -10-dB impedance bandwidth, the difference between them is no more than 0.7dB.

The measured co-polarized realized gain patterns normalized to their peak values 2.81, 2.92, and 3.28 dBi, respectively, at the indicated frequency points 27.74, 27.9 and 28.1 GHz, together with the corresponding HFSS and CST results, are given in Fig. 4. The measured realized gain patterns are stable across the operating bandwidth while the main-beam direction in the E-plane is slightly tilted. These differences are ascribed to three factors. First, a relatively long coaxial feed-line from the VNA was used in the measurements while a short one (with length 0.5 mm) was included in the simulations to model the actual transition between the dipole strips and the coax feed line. According to our simulations and confirmed by the fabricated samples, when the length of the feedline is longer than 50 mm, unbalanced surface currents appear on the metallic outer wall. These decrease the peak realized gain value ~ 0.74 dB, and make the radiation pattern tilt away from the end-fire direction in the *E*- (ZOX) plane while having little effect on the radiation pattern in the *H*- (ZOY) plane. Second, as was indicated previously, the incomplete overlap of the electric and magnetic NFRP element resonances caused by the fabrication and assembly issues also contributes to the differences between the simulated and measured realized gain values and radiation patterns observed in Fig. 4.

C. Simulated LP SAR Results

For health and safety purposes, the USA's Federal Communication Commission (FCC) has specified a 1.6 W/kg limit of the SAR averaged over any 1.0 g of tissue in the shape of a cube (1-g average SAR) below 6 GHz [35, 36]. However, the permissible SAR levels at mmWave frequencies have not yet been officially released, even though the mmWave cellular system has become a hot research topic in recent years [37]. In our studies, we used a Voxel Gustav human body in CST MWS

to evaluate the SAR values produced by the LP Huygens source ESA [38].

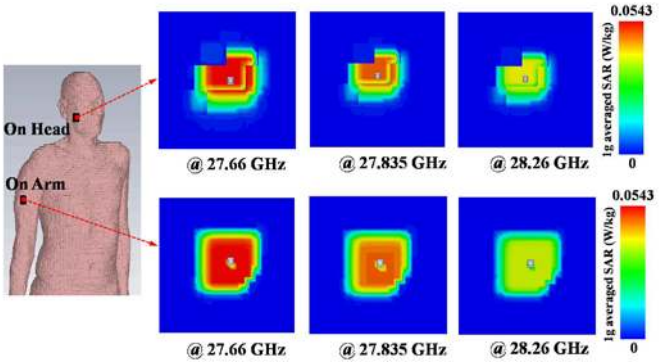

Fig. 5 Simulated 1g-averaged SAR values of the LP Huygens source ESA mounted on the head and the arm of the Voxel Gustav human body in CST MWS at several frequencies within its operational bandwidth.

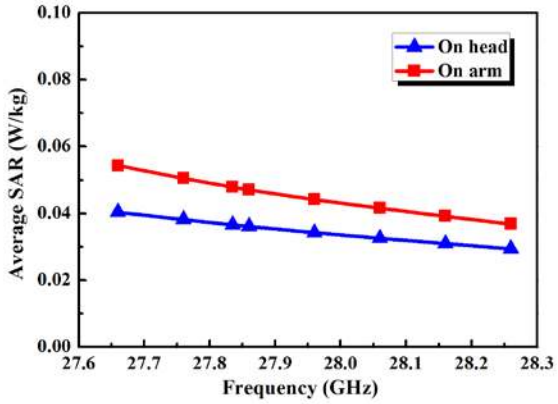

Fig. 6 Simulated peak 1g-averaged SAR values of the LP Huygens source ESA mounted on the head and the arm of the Voxel Gustav human body in CST MWS as a function of the frequencies within its operational bandwidth.

In order to simulate the SAR associated with the LP Huygens source ESA, it was placed on the skin of the head and arm of the Voxel Gustav human body in CST MWS. As a benchmark, the input power of the ESA was set to 1.0 W to evaluate its SAR performance. The simulated results for different antenna placements on the body at several frequencies within its operational bandwidth are shown in Figs. 5 and 6. During the CST simulations, it was observed that the presence of the body has little effect on the antenna performance. The 1g-averaged SAR values distributions are shown in Fig. 5 for head and arm positions at 27.66, 27.96, and 28.26 GHz. It is worth noting that the skin tissue is not smooth in the model; it is more like a stack of skin tissue blocks trying to reproduce the body shape. It makes the simulated 1g-averaged SAR values distributions in Fig. 5 not be gradual and smooth looking. Nevertheless, one observes that the SAR distributions in the head and arm both have their strongest values around the ESA and gradually become much weaker away from it. Furthermore, the peak 1g-averaged SAR values at a larger series of frequencies, from 27.66 to 28.26 GHz with steps of 0.1 GHz, are presented in Fig. 6. As the results in Figs. 5 and 6 indicate, the averaged SAR values are decreasing as the frequency increases. Furthermore, the peak average SAR values on the head and on the arm for all of the frequencies tested are below the maximum value: 0.0543 W/kg, which is substantially lower than 0.15 W/kg at 28GHz reported by *Samsung Electronics* [34].

III. CP HUYGENS SOURCE ESA

Based on the design principles learned through the development of the LP Huygens source ESA, a single-feed, broadside radiating, CP Huygens source ESA was engineered. All three components, both the NFRP elements and the driven element, had to be tailored to produce fields polarized in two orthogonal directions to achieve the desired CP performance. Further nuances had to be introduced to achieve a system well-matched to the source.

A. CP Design

The geometry of the CP Huygens source antenna is shown in Fig. 7. The final optimized parameters are given in Table II. The design also consists of four stacked pieces of the Rogers Duroid ™ 5880 substrate. However, they are all now circular in shape with the same radius R6 =1.5 mm, but with different thicknesses. The circular shape facilitates a smaller *ka* value of the final design.

Similar to the elemental arrangement in Fig. 1, the magnetic and electric NFRP elements are placed in the near field of the driven element, above its printed strips. Their phase centers are also adjusted to be aligned with each other. Again, this is the reason that the heights of the different layers (h1, h2, h3, and h4) in Figs. 1 and 7 are unequal. In order to achieve the CP operation, the configurations of the electric and magnetic NFRP elements and the driven element are quite different from, while nevertheless being very closely related to, their LP counterpart. The electric NFRP element now consists of two "I" elements oriented orthogonal to each other in the same plane (hence, it mimics a Jerusalem cross frequency selective surface unit element). Both lie on the lower surface of Layer_1, as is shown in Fig. 7(b). This basic structure, excited by a driven dipole element, has been used previously to produce two orthogonal resonances for CP operation [39]. Similarly, as shown in Fig. 7(c), the magnetic NFRP element now consists of four symmetrically placed, same-sized square patches on the lower surface of Layer_2. As illustrated in Fig. 7(a), they are connected to the square patch on the upper side of Layer_1 by four vertical metallic vias. Simply, this configuration is equivalent to two CLLs in an orthogonal arrangement. Such a system has been used previously to launch CP fields with the help of a driven element [40].

In addition to these straightforward combinations of LP designs, a rectangular cross slot is etched in the square patch on the upper side of Layer_1. This arrangement is highlighted in Fig. 7(b). The crossed slot was determined to have two functions: (1) it regulates the current pathway on the patch surface to improve the purity of the resulting CP radiation, and (2) it helps to adjust the capacitive coupling strength between

the magnetic NFRP element and the driven element. Hence, it intimately helps enhance the level of impedance matching.

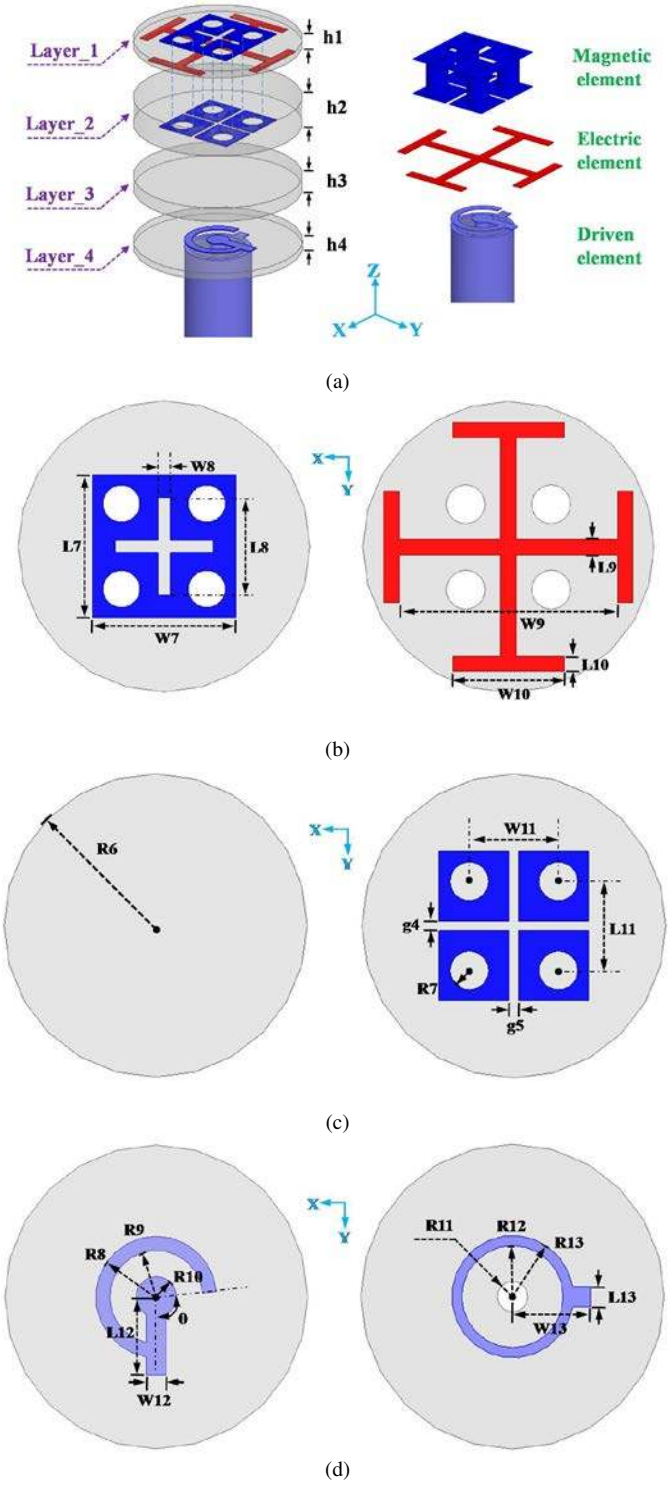

Fig.7 Geometry of the CP Huygens source ESA. (a) 3-D isometric view; (b) upper and lower surface of Layer_1; (c) upper and lower surface of Layer_2; and (d) upper and lower surface of Layer_4.

Finally, as shown in Fig. 7(d), the driven element is modified significantly. Although one rectangular strip is still directly connected to the outer wall of the 50Ω coaxial line on the bottom surface of Layer_4, the segment connected to its center conductor (it has the same diameter, 2.29 mm, as the LP version) on the top of Layer_4 has been modified to include a ring structure that facilitates the proper phase excitement of the two pairs of two orthogonal NFRP elements. Its rectangular piece is notably longer than and orthogonal to the one on the lower surface. It remains directly connected to the center conductor. The additional arc-shaped strip modification shifts the frequency at which the minimum AR value occurs to overlap with that of the minimum $|S_{11}|$ value. Its optimized total length was determined to be equivalent to θ = 100°.

TABLE II. OPTIMIZED CP HUYGENS SOURCE ESA PARAMETERS (IN MM)

h1=0.127	*h2=0.508*	*h3=0.254*	*h4=0.127*
L7=1.48	*L8=1*	*L9=0.16*	*L10=0.16*
L11=0.88	*L12=0.7*	*L13=0.18*	*W7=1.48*
W8=0.13	*W9=2.25*	*W10=1.14*	*W11=0.88*
W12=0.18	*W13=0.7*	*g4=0.09*	*g5=0.09*
R6=1.5	*R7=0.2*	*R8=0.6*	*R9=0.46*
R10=0.2	*R11=0.15*	*R12=0.5*	*R13=0.6*
θ =100 °	*NULL*		

B. Simulated CP Results

The simulated performance characteristics of the optimized CP Huygens source ESA were again obtained with both HFSS and CST. As shown in Fig. 8, the HFSS (CST) simulated -10-dB impedance bandwidth is 400 MHz, from 27.93 to 28.33 GHz (370 MHz, from 27.97 to 28.34 GHz) yielding FBW_{-10dB} ~1.43% (~1.31%). The predicted 3-dB axial ratio (AR) bandwidth is 130 MHz, from 28.04 to 28.17 GHz (120 MHz, from 28.07 to 28.19 GHz). The AR minimum value 1.18 dB (1.86 dB) occurs at 28.105 GHz (28.14 GHz). The overall electrical size of the HFSS (CST) model at the lowest frequency bound of the AR bandwidth is *ka* = 0.942 (0.943).

Within the 3-dB AR bandwidth, the FTBR values are higher than 20 dB (15dB) and their maximum value is 26.72 dB (17.9 dB) and is located at 28.11 GHz (28.14 GHz). The peak realized gain varies from 1.80 to 2.03 dBi (from 2.34 to 2.82 dBi). The RE values are contained in the range from 69.6 to 73.4% (from 71.5 to 74.5%). In comparison to the CP, helical-ring, Huygens source antenna reported in [41], with its complicated 3-D configuration and larger electrical size: *ka* = 1.13, the optimized CP Huygens source antenna reported here has a simpler, easier-to-fabricate multi-layer configuration and a much smaller electrical size.

The 2D realized gain patterns of the CP Huygens source ESA in both the zx and yz planes at 28.105 GHz are shown in Fig. 9. Clearly, the much larger co-pol results are in very good agreement. Moreover, both simulators predict quite low cross-pol levels. It also is obvious that both the HFSS and CST simulated results exhibit excellent broadside radiation patterns in both planes. At the operational center frequency, 28.105 GHz, the predicted broadside realized gain is 1.94 dBi (2.43 dBi) with a CP polarization purity higher than 20 dB (15 dB). The half-power beamwidth coverage is 180°, from -81° to 99° (167°, from -77° to 90°) in the zx-plane and 173°, from -93°

to 80° (158°, from -84° to 74°) in the yz -plane, respectively. The reason the design operates in a left-handed (LH) CP state is due to the arrangement of the arc-shaped strip, i.e., it has a clockwise rotation. Simulation results show that a right-handed (RH) CP Huygens source ESA is achieved simply by changing the rotation of the arc-shaped strip to be anti-clockwise.

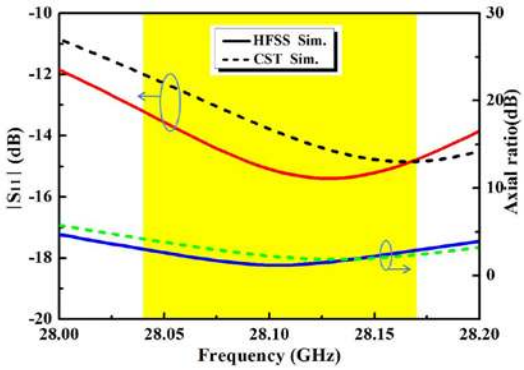

(a)

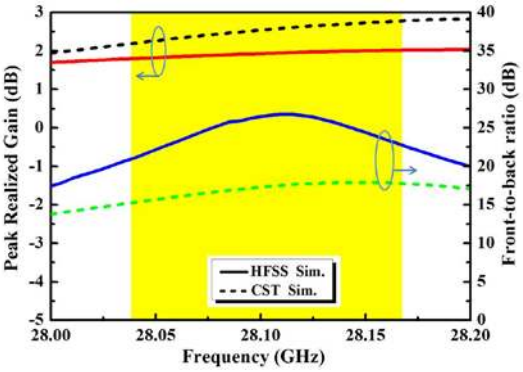

(b)

Fig. 8 The HFSS (solid line) and CST (dashed line) simulated performance characteristics of the CP Huygens source ESA. (a) $|S_{11}|$ and AR values, and (b) peak realized gain and FTBR values versus the source frequency. The HFSS simulated 3dB AR bandwidth range is shaded in yellow.

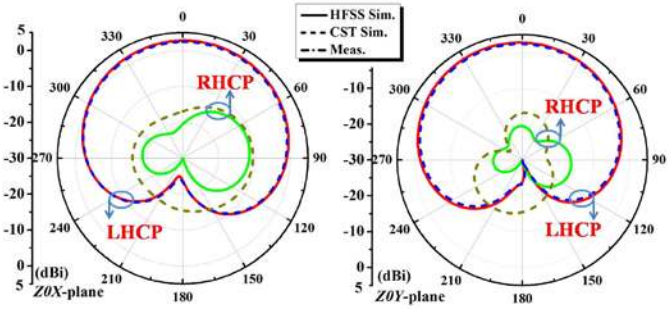

Fig. 9 The HFSS (solid line) and CST (dashed line) simulated 2D realized gain patterns of the optimized CP Huygens source ESA at its operational center frequency, 28.105 GHz, in the (a) zx and (b) yz planes.

C. Simulated CP SAR Results

Using CST MWS simulation parameters identical to those used for the evaluation of the SAR levels of the LP Huygens source ESA, the SAR values of the CP Huygens source ESA were obtained. These included the placements of the ESA and the mesh resolution size. The 1g-averaged SAR values of the CP Huygens source ESA were simulated. The results are shown in Figs. 10 and 11. Similar to the SAR distributions in Fig. 5, the 1g-averaged SAR distributions shown in Fig. 10 at a lower, middle, and upper frequency of its 3-dB AR band also witness uneven edges because of the discontinuity of the Voxel Gustav human body skin tissues. The peak 1g-averaged SAR values are shown in Fig. 11 as a function of the source frequencies within its 3dB AR operating bandwidth. Compared with the results in Fig. 6, the peak average SAR values within the 3dB AR operating bandwidth of the CP antenna are slightly higher than those of its LP counterpart. Nonetheless, its peak average SAR value is 0.0812, which is also much lower than the 0.15 W/kg specification [34]. Analogous to the LP version, the presence of the body has little effect on the simulated antenna axial ratio behavior.

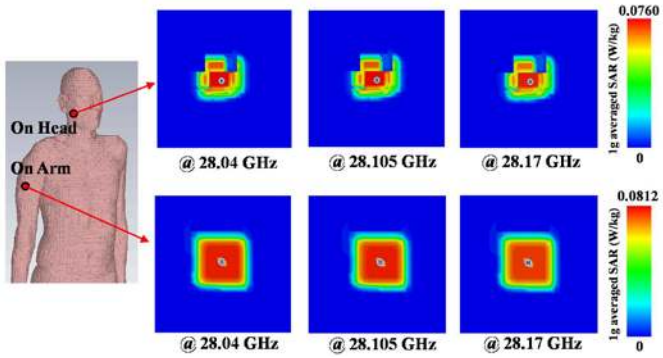

Fig. 10 Simulated 1g-averaged SAR values of the CP Huygens source ESA mounted on the head and the arm of the Voxel Gustav human body in CST MWS at several frequencies within its operational 3-dB AR bandwidth.

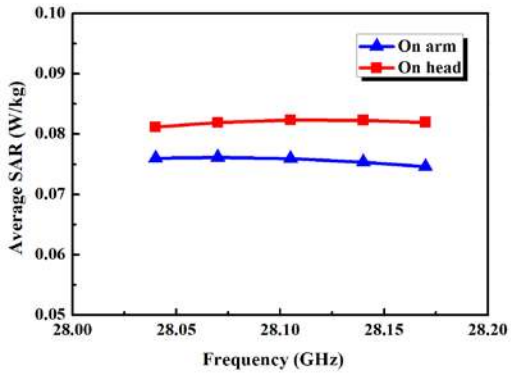

Fig. 11 Simulated peak 1g-averaged SAR values of the CP Huygens source ESA mounted on the head and the chest of the Voxel Gustav human body in CST MWS a function of the frequencies within its 3-dB AR operational bandwidth.

IV. Conclusion

Both LP and CP planar, multi-layer, broadside radiating, Huygens source ESAs based on multi-layer PCB technology operating in the mmWave 28 GHz band were demonstrated. Both designs consisted of an electric EAD NFRP element, a

magnetic CLL NFRP element, and a driven dipole element. It was established that by optimally engineering their sizes and shapes and arranging their relative positions, which was shown to be equivalent to adjusting the capacitively coupled current magnitudes on the NFRP elements and their phase centers, efficient Huygens source ESAs that radiate in their broadside direction were achieved. The simulated performance characteristics were obtained with two simulation environments, HFSS and CST MWS, and were shown to be in good agreement. The simulated SAR values were calculated with CST MWS; they were demonstrated to be much lower than current FCC limits defined for antennas operating in standard lower frequency bands. Benefitting from their advantages, including their easy-to-fabricate planar configurations, electrically small sizes, very good broadside radiating performance characteristics, and very low SAR values, these Huygens source ESAs should be very good candidates for mobile systems and wearable IoT devices operating in the near-future 28 GHz band, 5G systems.

REFERENCES

[1] R. F. Harrington, "Effect of antenna size on gain, bandwidth and efficiency," *J. Res. Nat. Bur. Stand*, vol. 64-D, pp. 1-12, Jan. / Feb. 1960.

[2] D. Xie, X. Liu , H. Guo , and Xinmi Yang, "Square electrically small EAD antenna array for RF energy harvesting from TV broadcast tower," *2014 Asia-Pacific Microwave Conference (APMC)*, Sendai, Japan, Nov. 4-7, 2014, pp.1357 – 1359.

[3] V. Jaeck, L. Bernard, K. Mahdjoubi, R. Sauleau, S. Collardey, P. Pouliguen, and P. Potier, "A conical patch antenna array for agile point-to-point communications in the 5.2-GHz band," *IEEE Antennas Wirel. Propag. Lett.*, vol. 15, pp. 1230-1233, 2016.

[4] P. Turalchuk, I. Munina, M. Derkach, O. Vendik, and I. Vendik, "Electrically small loop antennas for RFID applications," *IEEE Antennas Wirel. Propag. Lett.*, vol. 14, pp. 1786-1789, 2015.

[5] W. Xia; K. Saito, M. Takahashi, and K. Ito, "Performances of an implanted cavity slot antenna embedded in the human arm," *IEEE Trans. Antennas Propag.*, vol. 57, no. 4, pp. 894-899, Apr., 2009.

[6] T. S. Rappaport, S. Sun, R. Mayzus, H. Zhao; Y. Azar, K. Wang, G. N. Wong, J. K. Schulz, M. Samimi, F. Gutierrez, "Millimeter wave mobile communications for 5G cellular: It will work!" *IEEE Access*, vol. 1, no. 1, pp. 335-349, May 2013.

[7] W. Hong, K. H. Baek, Y. Lee, Y. Kim, and S. T. Ko, "Study and prototyping of practically large-scale mmWave antenna systems for 5G cellular devices," *IEEE Commun. Mag.*, vol. 52, no. 9, pp. 63-69, Sep. 2014.

[8] DM Center C. R. D., Samsung Electronics Co. Ltd., *5G Vision*, URL: http://www.samsung.com/global/business-images/insights/2015/Samsung-5G-Vision-0.pdf, Feb. 2015, accessed Sep. 2016.

[9] "mmWave: The battle of the bands," National Instruments, Jun. 09, 2016, http://www.ni.com/white-paper/53096/en/, accessed 20 Sep. 2016.

[10] "FCC Unanimously Opens Nearly 11 GHz of Spectrum for 5G," D. Goovaerts, 14 Jul. 2016, https://www.wirelessweek.com/news/2016/07/fcc-unanimously-opens-nearly-11-ghz-spectrum-5g, accessed 20 Sep. 2016.

[11] "T-Mobile 5G plans ensnare Samsung into 28 GHz trial," D. Meyer, RCR Wireless News, 07 Sep. 2016, http://www.rcrwireless.com/20160907/carriers/t-mobile-5g-plans-ensnare-samsung-28-ghz-trial-tag2, accessed 20 Sep. 2016.

[12] J. Ng, and R. W. Ziolkowski, "Combining metamaterial-inspired electrically small antennas with electromagnetic band gap (EBG) structures to achieve higher directivities and bandwidths," *Proc. 2012 International Workshop on Antenna Technology* (iWAT 2012), Tucson, America, March, 2012, pp. 189-192.

[13] M.-C. Tang, R. W. Ziolkowski, "Efficient, high directivity, large front-to-back-ratio, electrically small, near-field-resonant-parasitic antenna," *IEEE Access*, vol. 1, no. 1, pp. 16 - 28, May 2013.

[14] A. D. Yaghjian, T. H. O'Donnell, E. E. Altshuler, and S. R. Best, "Electrically small supergain end-fire arrays," *Radio Sci.*, vol.43, no. RS3002, pp. 1-13, 2008.

[15] A. Noguchi, and H. Arai, "3-element super-directive endfire array with decoupling network," in *Proc. 2014 International Symposium on Antennas and Propagation (ISAP)*, Kaohsiung, Taiwan, Dec. 2-5, 2014.

[16] A. D. Yaghjian, "Increasing the supergain of electrically small antennas using metamaterials," *in Proc. 3rd European Conference on Antennas and Propagation (EuCAP)*, Berlin, Germany, Mar. 23-27, 2009, pp. 858-860.

[17] S. R. Best, "Progress in the design and realization of an electrically small Huygens source," in *Proc. 2010 International Workshop on Antenna Technology (iWAT)*, Lisbon, Portugal, Mar. 1-3, 2010.

[18] P. Jin and R. W. Ziolkowski, "Metamaterial-inspired, electrically small Huygens sources," *IEEE Antennas Wirel. Propag. Lett.*, vol. 9, pp. 501-505, 2010.

[19] R. W. Ziolkowski, "Low profile, broadside radiating, electrically small Huygens source antennas," *IEEE Access*, vol. 3, pp. 2644-2651, Dec. 2015.

[20] P. Alitalo, A. O. Karilainen, T. Niemi, C. R. Simovski, and S. A. Tretyakov, "Design and realisation of an electrically small Huygens source for circular polarization," *IET Microwaves, Antennas & Propagation*, vol. 5, no. 7, pp. 783-789, 2011.

[21] T. Niemi, P. Alitalo, A. O. Karilainen, and S.A. Tretyakov, "Electrically small Huygens source antenna for linear polarization," *IET Microw. Antennas Propag.*, vol. 6, Iss. 7, pp. 735–739, 2012.

[22] K.-M. Luk, and B. Wu, "The magnetoelectric dipole: A wideband antenna for base stations in mobile communications," *Proc. IEEE*, vol. 100, no. 7, pp. 2297-2307, Jul. 2012.

[23] M. Li, and K.-M. Luk, "A low-profile, low-backlobe and wideband complementary antenna for wireless application," *IEEE Trans. Antennas Propag.*, vol. 63, no. 1, pp. 7-14, Jan. 2015.

[24] H.-J. Seo, and A. A. Kishk, "Wideband magnetic-electric antenna with linear single or dual polarization," *Progress In Electromagnetics Research (PIER)*, vol. 155, pp. 53-61, Mar. 2016.

[25] M.-C. Tang, H. Wang, and R. W. Ziolkowski, "Design and testing of simple, electrically small, low-profile, Huygens source antennas with broadside radiation performance," *IEEE Trans. Antennas Propag.*, vol. 64, no. 11, pp. 4607-4617, Nov., 2016.

[26] R. W. Ziolkowski, P. Jin, and C.-C. Lin, "Metamaterial-inspired engineering of antennas," *Proc. IEEE*, vol. 99, no. 10, pp. 1720-1731, Oct. 2011.

[27] M.-C. Tang, T. Shi, and R. W. Ziolkowski, "Electrically small, broadside radiating Huygens source antenna augmented with internal non-Foster elements to increase its bandwidth," *IEEE Antennas Wirel. Propag. Lett.*, DOI: 10.1109/LAWP.2016.2600525, 2016.

[28] N. Ojaroudiparchin, M. Shen, and G. F. Pedersen, "A 28 GHz FR-4 compatible phased array antenna for 5G mobile phone applications," *in Proc. IEEE Int. Symp. Ant. Propag.*, 2015, pp. 1 - 4.

[29] K. M. Morshed, K. P. Esselle, and M. Heimlich, "Dielectric loaded planar inverted-F antenna for millimeter-wave 5G hand held devices," *in Proc. 10th European Conference on Antennas and Propagation (EuCAP)*, 2016, pp. 1 - 3.

[30] ANSYS/ANSOFT High Frequency Structure Simulation (HFSS) ver. 13.0, ANSYS Corp. [Online]. Available: www.ansoft.com

[31] CST Microwave Studio CST of America, Inc. [Online]. Available: http://www.cst.com.

[32] Rogers RT/duroid™ 5870/5880 data sheet, Feb. 26, 2017 [Online]. Available: https://www.rogerscorp.com/documents/606/acs/RT-duroid-5870- 5880-Data-Sheet.pdf.

[33] M. J. Marcus, "5G and "IMT for 2020 and beyond", *IEEE Wireless Communications, Spectrum Policy and Regulatory Issues*, vol. 22, Iss. 4, pp. 2-3, 2015.

[34] W. Hong, K.-H. Baek, Y. Lee, Y. Kim, and S.-T. Ko, "Study and prototyping of practically large-scale mmWave antenna systems for 5G cellular devices," *IEEE Communications Magazine*, vol. 52, Iss. 9, pp. 63 -69, 2014.

[35] IEEE Standard for Safety Levels with Respect to Human Exposure to Radio Frequency Electromagnetic Fields, 3 kHz to 300 GHz, IEEE Standard C95.1-1999, 1999.

[36] C. Liu, Y.-X. Guo, H. Sun, and S. Xiao, "Design and safety considerations of an implantable rectenna for far-field wireless power transfer," *IEEE Trans. Antennas Propag.*, vol. 62, no. 11, pp. 5798-5806, Nov. 2014.

[37] T. Thomas, G. Charishma, and K. Veeraswamy, "MIMO antenna system with high gain and low SAR at for UE of 5G operating MM wave:

Design," *in Proc. 10th International Conference on Information, Communications and Signal Processing (ICICS)*, 2015, pp. 1 – 5.
[38] CST Microwave Suite Ver. 2012.08, CST Voxel Human Body Model. [Online]. Available: http:// www.cst.com.
[39] P. Jin, and R. W. Ziolkowski, "High-directivity, electrically small, low-profile near-field resonant parasitic antennas," *IEEE Antennas Wirel. Propag. Lett.*, vol. 11, pp. 305 - 309, 2012.
[40] C.-C. Lin, P. Jin, and R. W. Ziolkowski, "Multi-functional, magnetically-coupled, electrically small, near-field resonant parasitic wire antennas," *IEEE Trans. Antennas Propag.*, vol. 59, no. 3, pp. 714 - 724, Mar. 2011.
[41] C. Morlaas, B. Souny, and A. Chabory, "Helical-ring antenna for hemispherical radiation in circular polarization," *IEEE Trans. Antennas Propag.*, vol. 63, no. 11, pp. 4693-4701, Nov. 2015.

Ming-Chun Tang (S'12–M'13–SM'16) received the B. S. degree in physics from the Neijiang Normal University, Neijiang, China, in 2005 and the Ph. D. degree in radio physics from the University of Electronic Science and Technology of China (UESTC), in 2013. From August 2011 to August 2012, he was also with the Department of Electrical and Computer Engineering, The University of Arizona, Tucson, AZ, USA, as a Visiting Scholar. His research interests include electrically small antennas, RF circuits, metamaterial designs and their applications.

Prof. Tang was a recipient of the Best Student Paper Award in the 2010 International Symposium on Signals, Systems and Electronics (ISSSE2010) held in Nanjing, China. He is serving as a reviewer for IEEE/IET journals including the *IEEE Transactions on Antennas and Propagation, IEEE Transactions on Microwave Theory and Techniques, IEEE Antennas and Wireless Propagation Letters, IEEE Antennas and Propagation Magazine, IEEE Microwave and Wireless Components Letters, IEEE Access, IET Electronics Letters*, and *IET Microwaves, Antennas & Propagation*.

Ting Shi (S'16) received the B.S. degree from the University of Electronic Science and Technology of China (UESTC), Chengdu, China, in 2014. She is currently pursuing the M.S. degree in electronics and communication engineering in the College of Communication Engineering, Chongqing University, China.

Her current research interests include microwave antenna and filter designs and their applications.

Richard W. Ziolkowski (M'87–SM'91–F'94) received the B.Sc. (magna cum laude) degree (Hons.) in physics from Brown University, Providence, RI, USA, in 1974; the M.S. and Ph.D. degrees in physics from the University of Illinois at Urbana-Champaign, Urbana, IL, USA, in 1975 and 1980, respectively; and the Honorary Doctorate degree from the Technical University of Denmark, Kongens Lyngby, Denmark in 2012.

He is currently a Distinguished Professor with the University of Technology Sydney, Global Big Data Technologies Centre, Ultimo NSW, Australia. He is also a Litton Industries John M. Leonis Distinguished Professor with the Department of Electrical and Computer Engineering and a Professor with the College of Optical Sciences at The University of Arizona. He was the Computational Electronics and Electromagnetics Thrust Area Leader with the Lawrence Livermore National Laboratory, Engineering Research Division, before joining The University of Arizona, Tucson, AZ, USA, in 1990. He was the Australian DSTO Fulbright Distinguished Chair in Advanced Science and Technology from 2014-2015. He was a 2014 Thomas-Reuters Highly Cited Researcher. His current research interests include the application of new mathematical and numerical methods to linear and nonlinear problems dealing with the interaction of electromagnetic and acoustic waves with complex linear and nonlinear media, as well as metamaterials, metamaterial-inspired structures, and applications-specific configurations.

Prof. Ziolkowski is a Fellow of the Optical Society of America (OSA, 2006), and of the American Physical Society (APS, 2016). He served as the President of the IEEE Antennas and Propagation Society in 2005. He is also actively involved with the URSI, OSA and SPIE professional societies.